Hydrogen bonding steers the product selectivity of electrocatalytic CO reduction

Jingyi Li[a,1], Xiang Li[a,1], Charuni M. Gunathunge[a], and Matthias M. Waegele[a,2]

[a]Department of Chemistry, Merkert Chemistry Center, Boston College, Chestnut Hill, MA 02467

The product selectivity of many heterogeneous electrocatalytic processes is profoundly affected by the liquid side of the electrocatalytic interface. The electrocatalytic reduction of CO to hydrocarbons on Cu electrodes is a prototypical example of such a process. However, probing the interactions of surface-bound intermediates with their liquid reaction environment poses a formidable experimental challenge. As a result, the molecular origins of the dependence of the product selectivity on the characteristics of the electrolyte are still poorly understood. Herein, we examined the chemical and electrostatic interactions of surface-adsorbed CO with its liquid reaction environment. Using a series of quaternary alkyl ammonium cations (methyl$_4$N$^+$, ethyl$_4$N$^+$, propyl$_4$N$^+$, and butyl$_4$N$^+$), we systematically tuned the properties of this environment. With differential electrochemical mass spectrometry (DEMS), we show that ethylene is produced in the presence of methyl$_4$N$^+$ and ethyl$_4$N$^+$ cations, whereas this product is not synthesized in propyl$_4$N$^+$- and butyl$_4$N$^+$-containing electrolytes. Surface-enhanced infrared absorption spectroscopy (SEIRAS) reveals that the cations do not block CO adsorption sites and that the cation-dependent interfacial electric field is too small to account for the observed changes in selectivity. However, SEIRAS shows that an intermolecular interaction between surface-adsorbed CO and interfacial water is disrupted in the presence of the two larger cations. This observation suggests that this interaction promotes the hydrogenation of surface-bound CO to ethylene. Our study provides a critical molecular-level insight into how interactions of surface species with the liquid reaction environment control the selectivity of this complex electrocatalytic process.

hydrogen bonding | cation effects | electrocatalysis | carbon dioxide reduction | catalytic selectivity

The reaction environment profoundly impacts the kinetics of many chemical processes. Examples include the influence of the solvating environment on the rates of electron transfer (1), isomerization (2), peptide folding (3), and organic reactions (4), as well as the sensitivity of enzymatic catalysis to changes in the molecular structure of the active site (5). For a chemical process that can lead to multiple reaction products, solvent effects can impact the relative rates of product formation and therefore the product selectivity (6, 7). These effects, which can have complex energetic and/or dynamical origins (1, 8, 9), are fundamentally rooted in intermolecular interactions between the reactants and their environment. In the context of heterogeneous electrocatalysis, the reaction environment is asymmetric; i.e., reactants at the electrochemical interface are interacting with the solid electrode and the liquid electrolyte. Understanding the interactions of intermediates with their interfacial environment is essential for controlling the reaction paths of electrocatalytic processes that exhibit poor product selectivity.

The reduction of CO_2 to hydrocarbons on Cu electrodes in an aqueous environment is prototypical for a multielectron electrochemical process whose reaction selectivity is poor. Products include CO, formate, methane, ethylene, and alcohols (10–16). Hydrogen is a major product due to the competing water reduc-

tion reaction. This product spectrum sensitively depends on the properties of the electrocatalytic interface (17, 18). These properties are jointly determined by the liquid electrolyte and the solid electrode. Most research to date has focused on understanding how the chemical composition and the surface morphology of the electrode give rise to catalytic reactivity. For example, quantitative correlations have been established between catalytic selectivity and grain-boundary density (19–22), strain (23, 24), Cu nanocluster size (25–27), edge-site density (28–30), or single-crystal orientation (30–32). These observations have provided deep insights into the interactions of key reaction intermediates, such as CO, with the electrode surface and how these interactions impact product selectivity.

The reactants on the electrode also interact with the liquid side of the reaction environment. Solvent composition (33–36), the identity and concentration of the supporting electrolyte's anions (37–39) and cations (39–51), and the pH of the electrolyte (52–58) can greatly impact the product selectivity. For example, the rate of ethylene evolution during CO_2 reduction was found to increase by a factor of ≈ 15 when switching from Li$^+$- to Cs$^+$-containing electrolyte (47). Clearly, careful control of the liquid-side properties of the interface is critical for improving the product selectivity of this process. However, a molecular-level understanding of the interactions between surface reactants and their liquid reaction environment is largely lacking to date. This knowledge gap hinders the design of novel interfaces with desired product selectivity. An improved

Significance

Many technologically interesting electrocatalytic reactions lead to a variety of products; that is, they exhibit poor product selectivity. Examples include the oxidations of ammonia and methane and the reductions of nitrogen and carbon dioxide. The poor selectivity hinders the adoption of these promising technologies. Improving the selectivity requires a molecular-level understanding of the factors that control these reaction processes. Herein, we investigated how the liquid reaction environment impacts the selectivity of the reduction of CO to ethylene, a prototypical process for multielectron–proton transfer reactions. We show that the intermolecular interaction between surface-adsorbed CO and interfacial water is critical for the formation of ethylene. This mechanistic insight is expected to guide the design of electrocatalytic interfaces with high product selectivity.

understanding is expected to advance various design strategies, such as the decoration of the electrode surface with molecular cocatalysts (59–63).

Changing the cations of the electrolyte is a powerful means to alter the properties of the liquid reaction environment. Therefore, in principle, this method could be used as a tool for revealing selectivity-determining interactions between surface reactants and the electrolyte environment. However, cations can affect an electrocatalytic process in a number of different ways that are challenging to experimentally differentiate from each other. For example, cations can displace charged reactants from the interface and modulate the interfacial electric field, thereby altering the rates of electron transfer from the electrode to surface species (40–43, 64). More recently, density functional theory (DFT) calculations have shown that cations can impact the adsorption energy of reactants and/or the activation barriers of surface processes (39, 46, 47, 65, 66). Cations can also block reaction sites (37, 49, 67–71), chemically interact with surface species (72–76), modulate the interfacial pH (45, 50), and/or alter the structure of interfacial water (77, 78). Therefore, to unambiguously identify the principal interactions that alter the product selectivity, the number of possible interactions needs to be minimized by careful experimental design. Further, multimodal probes of the electrocatalytic interface need to be used.

Herein, using a series of quaternary alkyl ammonium cations ($alkyl_4N^+$), we systematically manipulated the interfacial properties of the aqueous electrolyte/polycrystalline Cu interface. We chose these cations for two reasons: First, the ionic radius of an $alkyl_4N^+$ cation increases with increasing alkyl chain length (79). This characteristic enabled us to tune the width of the electrochemical double layer and therefore the strength of the interfacial electric field for a given applied electrode potential. Second, compared with the more commonly used alkali cations in CO_2 reduction studies, the use of these cations minimizes the number of possible interactions: Alkali cations are Lewis acids and their Lewis acid hardness decreases by a factor of 3 when going from Li^+ to Cs^+ (80). Because of their Lewis acidity, hydrated alkali cations can buffer the interfacial pH (45, 50) and they could potentially chemically interact with intermediates such as surface-adsorbed CO (CO_{ads}) (81), which is a Lewis base. By contrast, $alkyl_4N^+$ cations are not Lewis acids and their bulky alkyl chains minimize the chance of chemical interactions between these cations and intermediates.

Using a combined differential electrochemical mass spectrometry (DEMS) and surface-enhanced infrared absorption spectroscopy (SEIRAS) approach, we probed the effect of these cations on the reduction of CO_{ads} to ethylene on the polycrystalline Cu electrode. The reduction of CO_{ads} corresponds to the potential-determining step in the electrochemical reduction of CO_2 to hydrocarbons (82–86). Understanding the influence of the liquid reaction environment on this process is therefore essential for developing a better mechanistic understanding of CO_2 reduction.

Using DEMS, we found that ethylene is produced in $methyl_4N^+$- and $ethyl_4N^+$-containing electrolytes, but ethylene is not formed in the presence of $propyl_4N^+$ and $butyl_4N^+$. With SEIRAS, we comprehensively analyzed the Cu/electrolyte interface. Irrespective of the identity of the $alkyl_4N^+$ cation of the electrolyte, we observed approximately the same CO-saturation coverage on the Cu electrode. This observation suggests that the cations do not block CO adsorption sites. Analyzing the dependence of the C≡O stretch frequency of CO_{ads} on applied electrode potential, we determined the electrochemical Stark tuning slopes and derived the potential-dependent interfacial electric fields in the presence of the four cations. At moderate applied potentials around −1.3 V vs. the standard hydrogen electrode (SHE), the interfacial electric field is on the order of $0.1\ V\cdot Å^{-1}$. On the basis of a simple electrostatic model, we found that the interfacial electric field does not appreciably affect the adsorption of CO on Cu under the experimental conditions used in this work.

Analyzing the O−D stretch band of interfacial heavy water (D_2O) at the CO-covered Cu electrode, we found evidence for a layer of waters directly on top of CO_{ads} in $methyl_4N^+$- and $ethyl_4N^+$-containing electrolytes. These waters have their O−D bonds directed toward the terminal oxygens of the CO_{ads} molecules. Interestingly, this layer of waters is displaced by $propyl_4N^+$ and $butyl_4N^+$. These observations suggest that the $CO_{ads}−D_2O$ interaction is essential for the formation of ethylene during the electrochemical reduction of CO. These waters are predisposed to stabilize the CO dimer, a key intermediate in ethylene formation, by hydrogen bonding to its terminal oxygens. Theoretical work has recently predicted that this hydrogen-bonding interaction is critical for the formation of this important intermediate (87). Our findings are an experimental demonstration of the impact of this interaction on the selectivity of CO reduction.

Results and Discussion

Effects of Alkyl$_4$N$^+$ Cations on CO Reduction. With DEMS, we analyzed the product selectivity during the electrocatalytic reduction of CO to ethylene on polycrystalline Cu electrodes in four different electrolytes. The electrolytes were aqueous solutions of $methyl_4N^+$, $ethyl_4N^+$, $propyl_4N^+$, and $butyl_4N^+$ borates (0.1 M) and EDTA disodium (EDTA-Na_2; 20 μM). EDTA-Na_2 prevents deactivation of the electrocatalytic interface by chelating trace metal impurities (88). The electrolytes had a pH of 9.5, which is close to the pK_a of boric acid (9.24). Therefore, the solutions were pH buffered by the acid–base equilibrium between the anion (borate) and boric acid. Before the start of a DEMS measurement, the electrolyte was first saturated with CO. A 5 standard cubic centimeters per minute (sccm) flow rate of CO was maintained throughout the experiment. Detailed experimental procedures are given in *Materials and Methods*, and a scheme of the DEMS setup is provided in *SI Appendix*, Fig. S1.

Fig. 1 shows the electrochemical current and the partial pressures of the two major products, hydrogen and ethylene, following two potential steps. The products were identified by their characteristic mass fragment/charge ratios (m/z) of 2 for H_2^+ and 26 for $C_2H_2^+$. Unless otherwise noted, all potentials in this work are referenced against the SHE. The voltage was first stepped from −0.39 V to −1.09 V (Fig. 1, light gray shaded area), the potential at which the CO-saturation coverage on the Cu electrode is IR-spectroscopically observed (below). After holding this voltage for 1 min, the potential was decreased at a rate of 10 mV·s^{-1} to −1.29 V, which was maintained for 5 min (Fig. 1, dark gray shaded area). As shown in Fig. 1A, comparable electrochemical current densities are observed in the presence of $methyl_4N^+$, $ethyl_4N^+$, and $propyl_4N^+$, while an ≈30% lower current is observed in the presence of $butyl_4N^+$. The hydrogen partial pressure (Fig. 1B) detected by DEMS closely follows these trends, suggesting that hydrogen is the major reduction product. As shown in Fig. 1C, ethylene is observed in $methyl_4N^+$- and $ethyl_4N^+$-containing electrolytes, but this product is not observed in the presence of the two larger cations.

Like similar setups (48, 89), our DEMS instrument is not capable of making fully quantitative measurements of the reaction rates: The product collection efficiency is dependent on the tip–electrode distance, which is difficult to accurately reproduce between independent experiments. Due to the low solubility of CO in water (≈1 mM), the measured rates may also be limited by mass transport of CO to the electrode. Despite these

Fig. 1. DEMS measurements. (*A*) Electrochemical current density based on the geometric area of the electrode, (*B*) H$_2$ partial pressure ($m/z = 2$ for H$_2^+$), and (*C*) C$_2$H$_4$ partial pressure ($m/z = 26$ for C$_2$H$_2^+$) recorded during the electroreduction of CO on Cu in the presence of different cations as indicated. The sequence of potential steps in these experiments is described in the main text.

limitations, we could reproducibly determine that ethylene is formed at detectable rates in the presence of methyl$_4$N$^+$ and ethyl$_4$N$^+$, whereas we did not observe any ethylene in propyl$_4$N$^+$- and butyl$_4$N$^+$-containing electrolytes.

To confirm that the observed signal at $m/z = 26$ is due to ethylene formed by the reaction of CO and water at the

Cu electrode, we carried out a series of control experiments: No ethylene signal ($m/z = 26$) is detected in the presence of methyl$_4$N$^+$ in Ar-purged electrolyte (*SI Appendix*, Fig. S2) or in CO-purged methyl$_4$N$^+$-containing electrolyte when the electrode material is Pt (*SI Appendix*, Fig. S3). Further, ethylene and hydrogen evolution is virtually unchanged when switching from methyl$_4$N$^+$ to its deuterated form, (CD$_3$)$_4$N$^+$ (*SI Appendix*, Fig. S4).

These experiments conclusively demonstrate that the appearance of the $m/z = 26$ signal not only requires the presence of CO, but also necessitates the presence of a Cu electrode. Cu is the only pure metal that can reduce CO to ethylene at appreciable rates (13, 90, 91). Therefore, the absence of this signal when a Pt electrode is used strongly supports its assignment to the C$_2$H$_2^+$ mass fragment of ethylene. Further, the experiments demonstrate that the signal is not due to the decomposition of the organic cations or their reaction with CO$_{ads}$.

To confirm this assignment further, we examined the mass spectrum. Because some reactants and products yield ions with m/z values that overlap with the mass spectrum of ethylene (e.g., CO$^+$ and C$_2$H$_4^+$ both have $m/z = 28$), its full mass spectrum cannot be observed during a DEMS measurement. However, ethylene's m/z values of 25, 26, and 27 do not overlap with the mass spectra of any other major reduction product of CO on copper. As shown in *SI Appendix*, Fig. S5, the observed relative partial pressures at these three m/z values are in good agreement with those expected for ethylene. In addition, we confirmed the identity of ethylene with gas chromatography/mass spectrometry (GC-MS). An experiment with ^{13}C-labeled CO unequivocally established CO as the sole source of ethylene (*SI Appendix*, Fig. S6).

Alteration of molecular diffusion coefficients by the cations could result in cation-dependent product collection efficiencies. However, the comparable decay times of the hydrogen partial pressure (Fig. 1*B*) following the step from −1.39 V to −0.39 V at $t \approx 6.3$ min suggest that molecular diffusion coefficients are similar in the four electrolytes. Taken together, the data unambiguously demonstrate that the identity of the alkyl$_4$N$^+$ cation of the electrolyte profoundly influences the selectivity of the CO reduction process on the polycrystalline Cu electrode.

SEIRAS of the Cu/Electrolyte Interface. To identify the principal mechanism giving rise to the observed selectivity trend, we characterized the Cu/electrolyte interface under operating conditions, using SEIRAS in an attenuated total reflection (ATR) geometry. An electrolessly deposited polycrystalline Cu film on a Si ATR prism (55, 92, 93) formed the working electrode of a single-compartment spectro-electrochemical cell (*SI Appendix*, Fig. S7). Characterization of the Cu film by cyclic voltammetry, capacitance measurements (*SI Appendix*, Fig. S8), and atomic force microscopy imaging (*SI Appendix*, Fig. S9) is reported in *SI Appendix*.

We carried out the spectroscopic work in solutions of the chloride salts of the alkyl$_4$N$^+$ cations in heavy water (D$_2$O). Primarily, we chose these electrolyte conditions for the following reason: With increasing current density, the Cu thin films have an increasing propensity to delaminate from the Si crystal (55). A significant component of the faradaic current originates from the hydrogen evolution reaction. To minimize the interference of hydrogen evolution with interfacial spectroscopy, we chose D$_2$O as the solvent. Due to the kinetic isotope effect, hydrogen evolution on Cu is substantially slower in D$_2$O compared with H$_2$O (94). For DEMS, alkyl$_4$N$^+$ borate electrolytes were prepared by titration of the corresponding hydroxide solutions (*Materials and Methods*). Because alkyl$_4$N$^+$ hydroxides are available only as H$_2$O solutions, we could not use this electrolyte preparation procedure for the spectroscopic experiments. Therefore, we chose to directly dissolve alkyl$_4$N$^+$ chlorides in D$_2$O. The pH of these

solutions slightly drifts during the measurements (*Materials and Methods*). It is well established that adsorption of CO on Cu is pH independent (55, 95). Further, our previous work established that the CO stretch frequency is only slightly affected by pH (95). Therefore, the following analyses are not impacted by this choice of electrolyte.

To connect rigorously the DEMS and spectroscopic experiments, we carried out the following control experiments: (*i*) DEMS results qualitatively similar to those presented above are also found in aqueous solutions of $alkyl_4N^+$ chlorides (*SI Appendix*, Fig. S10). We emphasize that we compare only the qualitative trends because the reversible hydrogen electrode (RHE) potential is not well defined in the latter measurements. (*ii*) Additional spectroscopic experiments were carried out under electrolyte and potential conditions identical to those used for the DEMS experiments (*SI Appendix*, Fig. S11). These experiments confirm that the cation-dependent trends in the $CO_{ads}-H_2O$ interaction hold for both electrolytes (below). In the following, we evaluate the effects of the cations on CO surface coverage, interfacial electric field, and interfacial water structure.

Insensitivity of the CO Surface Coverage on Alkyl₄N⁺ Identity. Fig. 2 shows representative spectra of the C≡O stretch band of CO_{ads} during a potential sweep from −0.39 V to −1.39 V collected in $butyl_4N^+$-containing electrolyte. Additional spectra collected in the presence of the other cations and the corresponding current densities are provided in *SI Appendix*, Figs. S12 and S13.

Fig. 3 shows the dependence of the integrated C≡O stretch band area of CO_{ads} on applied potential in the presence of the
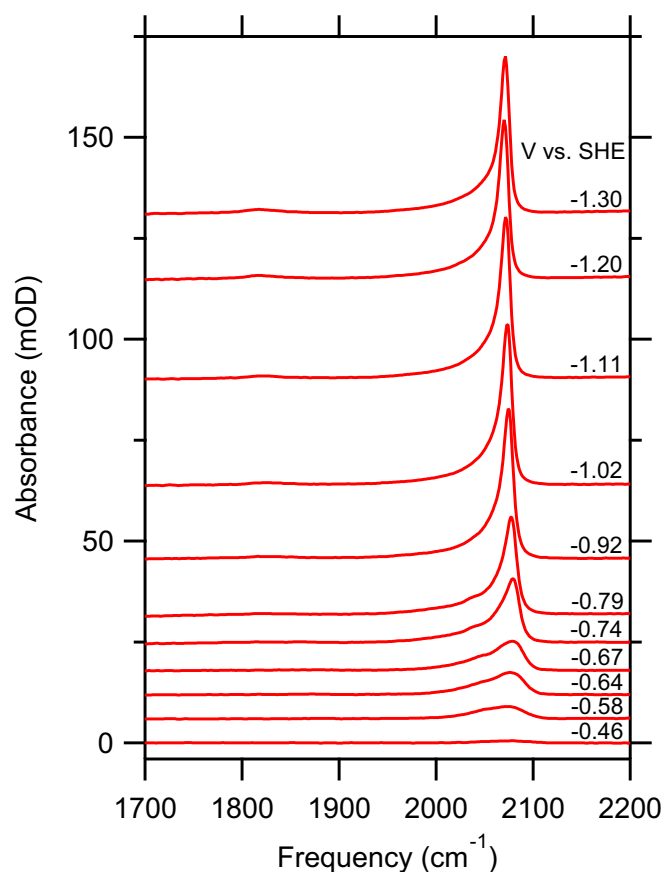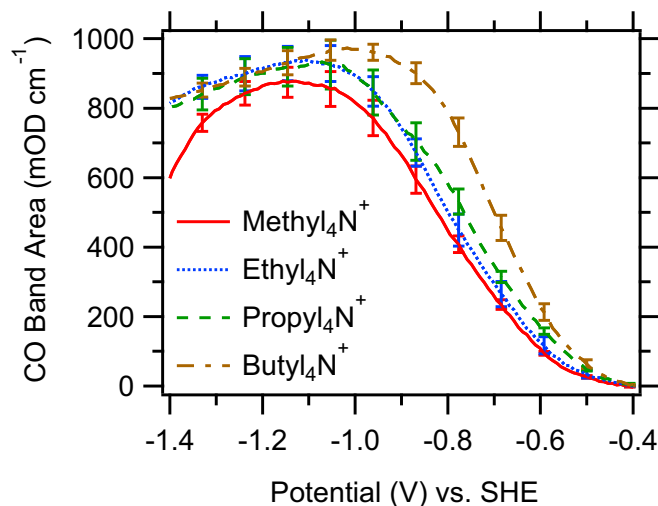
Fig. 3. Integrated C≡O stretch band areas of CO_{ads} as a function of applied potential in the presence of different cations as indicated. Each trace is an average of three independent experiments. The standard errors are indicated.

different $alkyl_4N^+$ cations. The integrated C≡O stretch band area is approximately proportional to the CO coverage on the electrode (96, 97). Irrespective of the $alkyl_4N^+$ cation of the electrolyte, comparable integrated band areas are observed, indicating that the same CO-saturation coverage is reached within the error of the measurement. It was suggested that organic cations, especially those with long hydrocarbon chains, may displace reactants from the electrode surface under certain conditions (37, 68). Apparently, the Cu/CO interaction is sufficiently strong (compared with the Cu/$alkyl_4N^+$ interaction) to prevent such displacement effects. Further, in contrast to recent findings of CO on Pt electrodes (98), no displacement of a top-bound CO (center frequency ≈2,080 cm⁻¹) to the bridge-bonded configuration [center frequency ≈1,800−1,880 cm⁻¹ (99)] is observed (Fig. 2 and *SI Appendix*, Fig. S12). The results demonstrate that the changes in the rate of ethylene evolution with cation identity are not due to blocking of CO adsorption sites.

Cation-Dependent Interfacial Electric Field. Fig. 4 shows the dependence of the peak frequency of the C≡O stretch band of CO_{ads} on applied potential. To minimize coverage-dependent frequency shifts (100), the analysis was restricted to a potential range in which the CO coverage is approximately constant. The dependence of the frequency (ω) on the applied potential (ϕ) arises from the vibrational Stark effect, i.e., the influence of the interfacial electric field ($\mathcal{E}(\phi)$) on the C≡O stretch mode (101–104)

$$\omega(\phi) = \omega_{PZC} - \Delta\mu\, \mathcal{E}(\phi),\quad [1]$$

where ω_{PZC} (PZC, potential of zero charge) is the C≡O stretch frequency in the absence of the interfacial electric field and $\Delta\mu$ represents the vibrational Stark tuning rate. By writing $\Delta\mu$ and $\mathcal{E}$ in Eq. **1** as scalar quantities, we implicitly assumed that the corresponding vectors are either parallel or antiparallel to each other. This assumption is reasonable for CO adsorbed on a metal surface (105). However, it is an approximation as our electrodes are not atomically flat. We take $\Delta\mu$ and $\mathcal{E}$ as positive quantities when the corresponding vectors point from the electrolyte toward the metal surface. The $\Delta\mu$ vector of CO_{ads} points from O to C.

The vibrational Stark tuning rate for CO adsorbed on Cu is 1.3×10^{-6} cm⁻¹/(V·cm⁻¹) (106). Although this value was

Fig. 2. Representative C≡O stretch spectra of CO_{ads} as a function of applied potential in the presence of a solution of 0.1 M butyl₄N⁺ chloride in D_2O.
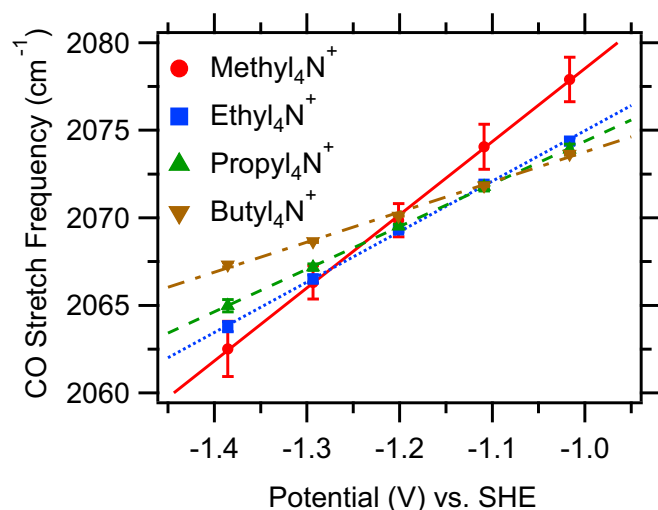
Fig. 4. Peak frequencies of the C≡O stretch band of CO_{ads} as a function of applied potential in the presence of different cations as indicated. The lines are linear fits to the data. The standard errors are indicated.

derived from quantum mechanical calculations of CO on a Cu surface in vacuum, very similar values were estimated for CO adsorbed on various metal electrodes in an aqueous environment (105). Further, experimental measurements of $\Delta\mu$ for CO adsorbed on various metals in vacuum also yielded comparable values (105).

The data in Fig. 4 contain information on the structure of the electrochemical double layer. Inspection of Fig. 4 shows that the frequency linearly depends on the applied potential. This observation implies that the interfacial electric field is also linearly related to the applied potential (Eq. **1**). One model of the electrochemical double layer that is consistent with this finding is the Helmholtz model (107)

$$\mathcal{E}(\phi) = -\frac{\Delta\phi_{M-El}}{d_H}, \qquad [2]$$

where $\Delta\phi_{M-El}$ is the interfacial potential drop, $\phi_M - \phi_{El}$ (ϕ_M and ϕ_{El} are the potentials of the metal and the bulk electrolyte, respectively). d_H is the width of the Helmholtz layer, i.e., the distance between the negatively charged electrode surface and the plane of the cationic counter charge (outer Helmholtz plane). Combining Eqs. **1** and **2**, we obtain

$$\omega(\phi) = \omega_{PZC} + \left(\frac{\Delta\mu}{d_H}\right)\Delta\phi_{M-El}. \qquad [3]$$

The width of the Helmholtz layer (d_H) is expected to increase with increasing cation size: With increasing cation size, the outer Helmholtz plane shifts farther away from the electrode surface. Consistent with this expectation, the slopes of the lines in Fig. 4, the electrochemical Stark tuning rates ($\Delta\mu/d_H$) (81, 108, 109), decrease with increasing cation size (Table 1). One may expect the extracted values of d_H to track the ionic radii of the cations. The radii of the cations [derived from the partial molar volumes of the cations in water (79)] are 3.2 Å, 3.8 Å, 4.4 Å, and 4.7 Å for $methyl_4N^+$, $ethyl_4N^+$, $propyl_4N^+$, and $butyl_4N^+$, respectively. The extracted width increases at a larger rate with increasing cation size (Table 1) than that expected based on the radii of the cations. This observation suggests that the smaller cations fit between CO_{ads} molecules on the surface. This interpretation is reasonable because the CO-saturation coverage on Cu electrodes is estimated to be significantly less than one monolayer (39). By contrast, the larger cations appear to reside at a distance

from the electrode approximately equal to the distance between the surface of the electrode and the terminal oxygen of CO_{ads} [3.05 Å (110)] plus the radius of the cation. Clearly, based on Eq. **2**, we therefore expect the interfacial electric field to decrease with increasing cation size for the same applied potential.

To extract the interfacial electric field from Eq. **1**, knowledge of the C≡O stretch frequency of CO_{ads} in the absence of the field (ω_{PZC}) is required. The interfacial electric field strength vanishes at the PZC of the electrode. This potential can be estimated from Fig. 4 (109). Inspection of Fig. 4 shows that the lines obtained for $ethyl_4N^+$-, $propyl_4N^+$-, and $butyl_4N^+$-containing electrolytes cross at ≈ -1.1 V. This crossing point indicates that CO_{ads} experiences the same interfacial electric field at this potential, irrespective of the electrolyte's cation. This condition can be fulfilled only when the electrode does not carry any net charge, i.e., when $\Delta\phi_{M-El} = 0$ V (Eq. **3**). Therefore, this crossing point is the approximate PZC of the CO-covered Cu electrode in $alkyl_4N^+$ chloride solutions. This PZC is more negative than the values obtained on Cu electrodes in contact with acidic and weakly adsorbing electrolytes (≈ -0.73 V; pH 5.7; 0.01 M $NaClO_4$) (111). The more negative value obtained here is consistent with the expectation that the PZC shifts negatively by ≈ 60 mV per 1 unit increase in pH (112). Additionally, the specific adsorption of Cl^- on Cu may contribute to the more negative value.

The frequency/potential relationship obtained in the presence of $methyl_4N^+$ does not cross with the other lines at ≈ -1.1 V (Fig. 4). Although the measurement of the electrochemical Stark tuning slope in the presence of this cation was highly reproducible, the value of the y-axis intercept varied by as much as ≈ 5 cm^{-1} over independent experiments. Although the Cu thin films were stable for all of the presented measurements, we noticed a higher propensity of film delamination in the presence of $methyl_4N^+$. Therefore, this cation may interact more strongly with the electrode than the other ones in this series. Because even a significant error of 0.2 V in the value of the PZC will not change our conclusions drawn from the analysis that follows, we assume a PZC of ≈ -1.1 V of the Cu electrode for all of the four cations.

Using the extracted PZC and $\Delta\mu$, we evaluated the interfacial electric field ($\mathcal{E}$) according to Eq. **1**. We emphasize that the relationship between $\omega(\phi)$ and $\mathcal{E}(\phi)$ as defined in Eq. **1** does not require the assumption of a particular model of the electrochemical double layer. Fig. 5 shows the interfacial electric field experienced by CO_{ads} in the presence of different cations. The interfacial field decreases by a factor of ≈ 2.5 when going from $methyl_4N^+$- to $butyl_4N^+$-containing electrolyte. The obtained interfacial fields are on the order of 0.1 V·Å^{-1}. The electrostatic contribution to the CO-adsorption energy as a function of the local field is (46, 113)

$$E(\mathcal{E}) \approx -\mu\mathcal{E} - \frac{\alpha}{2}\mathcal{E}^2, \qquad [4]$$

where μ and α are the dipole moment and polarizability of CO_{ads}, respectively. CO is only weakly adsorbed on Cu and

Table 1. Electrochemical Stark tuning rates ($\Delta\mu/d_H$) extracted from fitting a linear model to the data in Fig. 4 and derived Helmholtz double-layer widths (d_H)

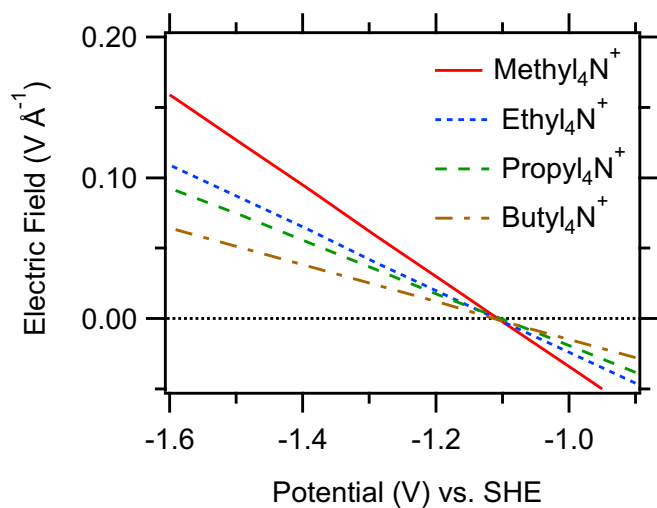| Cation	$\Delta\mu/d_H$, V^{-1}·cm^{-1}	d_H, Å
Methyl$_4$N$^+$	41.8 ± 0.6	3.1 ± 0.0
Ethyl$_4$N$^+$	28.8 ± 0.4	4.5 ± 0.1
Propyl$_4$N$^+$	24.3 ± 0.2	5.4 ± 0.0
Butyl$_4$N$^+$	17.2 ± 0.6	7.6 ± 0.3

The SDs are indicated.

Fig. 5. Dependence of the interfacial electric fields on applied potential in the presence of different electrolyte cations as indicated.

therefore is expected to exhibit little change in its dipole moment and polarizability with respect to the values of CO in the gas phase. With the gas-phase values of 0.0244 eÅ and 0.124 eÅ$^2\cdot$V^{-1} for the dipole moment and polarizability of CO (114), respectively, and an applied potential of -1.3 V, Eq. **4** predicts a minute change in the CO adsorption energy of <5 meV, which is negligible with respect to the adsorption energy of CO on Cu [≈ -0.6 eV (115, 116)].

The results suggest that the interfacial field at the Cu/electrolyte interface under the experimental conditions used in this work is too small to have a significant effect on the CO adsorption energy. This conclusion is consistent with DFT calculations demonstrating that an electric field of 0.1 V$\cdot$Å^{-1} has negligible effect on the adsorption energy of CO on Cu (99).

The interfacial electric field will affect the rate of electron transfer from the electrode to surface intermediates (64, 107). However, ethylene is also not observed in the presence of butyl$_4$N$^+$ when a potential of -1.39 V is applied (*SI Appendix,* Fig. S10). This observation demonstrates that, in the present case, the cation-specific selectivity for ethylene is likely unrelated to the strength of the interfacial electric field.

Dependence of the CO$_{ads}$–H$_2$O Interaction on Cation Identity. Interfacial water is the source of hydrogen in the electroreduction of CO$_{ads}$ and provides the solvation environment for the reactants. Therefore, the structure and dynamics of interfacial water are expected to affect this process. To determine whether the cations alter the structure of water near the electrode surface, we analyzed the dependence of the O–D stretch band of interfacial water at the CO-covered Cu electrode on the presence of the different cations (Fig. 6). In the presence of methyl$_4$N$^+$ and ethyl$_4$N$^+$, a sharp and prominent band is observed at $\approx 2,710$ cm^{-1} on top of the broad O–D stretch band. The band is very weak in the presence of propyl$_4$N$^+$ and it is entirely absent in butyl$_4$N$^+$-containing electrolyte. To confirm that these trends are also observable under electrolyte conditions identical to those used in the DEMS study, we collected spectra in H$_2$O solutions of methyl$_4$N$^+$ and butyl$_4$N$^+$ borates. As shown in *SI Appendix,* Fig. S11, the spectrum collected in the presence of methyl$_4$N$^+$ borate exhibits a sharp band at $3,675$ cm^{-1}. The position of the band is in good agreement with the isotopic shift that is expected on the basis of a simple harmonic oscillator model of the O–D/H stretch mode. By contrast, the band is absent in solutions of butyl$_4$N$^+$ borate (*SI Appendix,* Fig. S11).

These observations establish that the trends are also observable under the electrolyte conditions used in the DEMS study.

Prior reports established that this band arises from interfacial waters that directly interact with CO$_{ads}$ (78, 92, 117–121). These waters, which are not directly adsorbed on the electrode surface, have their O–D bonds pointed toward the terminal oxygen of CO$_{ads}$ (78, 119). The integrated area of this band tracks the CO surface coverage (*SI Appendix,* Fig. S15). Further, the band is absent in Ar-purged methyl$_4$N$^+$-containing electrolyte (*SI Appendix,* Fig. S16). These findings confirm that the band originates from interfacial waters that interact with CO$_{ads}$.

The center frequency of this band is slightly red shifted by a few tens of wavenumbers with respect to the frequency of the O–D stretch of an isolated water molecule (118, 120). On the basis of this observation, the interaction of water with CO$_{ads}$ is often considered to be weak (78, 119) compared with the hydrogen bonding in bulk water. However, it was shown that this interaction affects the electronic structure of the metal–CO bond (120), and it was suggested that the CO$_{ads}$–H$_2$O interaction may be stronger than previously assumed (121). Irrespective of this debate, our observations suggest that the two larger cations disrupt the CO$_{ads}$–H$_2$O interaction. Due to their larger size and more hydrophobic nature compared with methyl$_4$N$^+$ and ethyl$_4$N$^+$, they are expected to be more effective in displacing water molecules from the interface (77, 78).

Our findings suggest that ethylene evolution is shut down in the presence of propyl$_4$N$^+$ and butyl$_4$N$^+$ due to the disruption of the CO$_{ads}$–H$_2$O interaction by these two cations. At moderate overpotentials and basic pH, computational models (84–87, 122) and experimental evidence (48, 123) have suggested a surface-adsorbed CO dimer as an important intermediate in this reaction. Recent computational work predicts that hydrogen bonding of interfacial waters to the oxygens of the CO dimer is required for its formation to be energetically favorable (87). On the basis of these findings, we propose CO dimerization is impeded in the presence of propyl$_4$N$^+$ and butyl$_4$N$^+$ because these cations displace the water layer on top of CO$_{ads}$. Due to this displacement, these waters are not available to stabilize the CO dimer by hydrogen bonding to its terminal oxygens (Fig. 7). This picture is also consistent with the
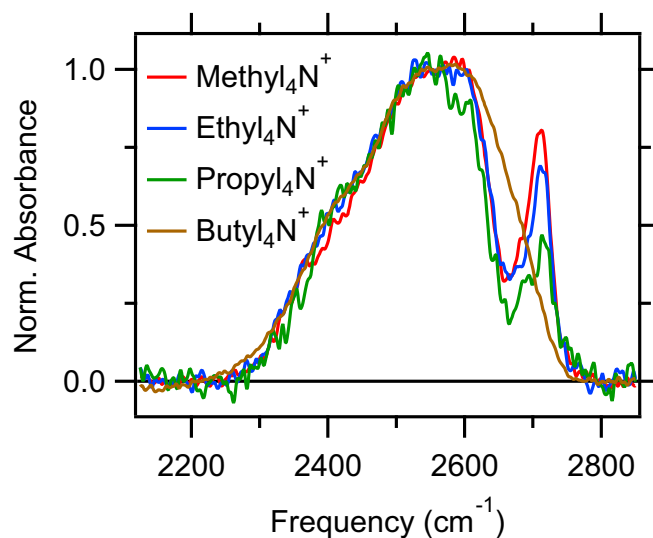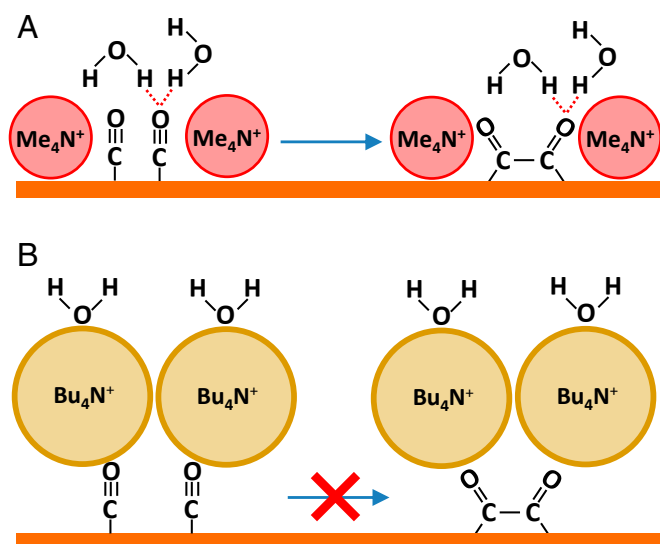

Fig. 6. Normalized O–D stretch spectra recorded at a potential of -1.02 V in the presence of different cations as indicated. The unnormalized spectra are provided in *SI Appendix,* Fig. S14.

Fig. 7. Possible CO$_{ads}$ coupling mechanism on Cu(100), as proposed by Bagger et al. (87). (*A*) In the presence of methyl$_4$N$^+$ (or ethyl$_4$N$^+$), interfacial waters are available to stabilize the CO dimer by hydrogen bonding. (*B*) In the presence of butyl$_4$N$^+$ (or propyl$_4$N$^+$), the formation of the CO dimer is blocked due to the displacement of interfacial water by these hydrophobic cations.

cation-dependent structure of the double layer (Table 1). Our study provides an experimental indication that this hydrogen-bonding interaction is indeed critical for CO dimerization on Cu electrodes.

Conclusions

We investigated the effects of alkyl$_4$N$^+$ on the electroreduction of CO to ethylene on the polycrystalline Cu electrode in aqueous electrolytes. Using DEMS, we showed that ethylene is produced in the presence of methyl$_4$N$^+$ and ethyl$_4$N$^+$, but this product is not observed in propyl$_4$N$^+$- and butyl$_4$N$^+$-containing electrolytes. Using SEIRAS, we comprehensively characterized the properties of the electrocatalytic interface in the presence of the four alkyl$_4$N$^+$ cations. Our spectroscopic results suggest that the change in ethylene selectivity does not arise from blocking of CO adsorption sites or cation-dependent changes in the interfacial electric field strength. Analysis of the O—D stretch band of interfacial heavy water (D$_2$O) at the CO-covered electrode revealed a sharp band at $\approx$2,710 cm^{-1} in methyl$_4$N$^+$- and ethyl$_4$N$^+$-containing electrolytes. This band, which is due to water with its O—D bond directed toward the terminal oxygen of CO$_{ads}$, is weak in the presence of propyl$_4$N$^+$ and entirely absent in butyl$_4$N$^+$-containing electrolyte. This observation demonstrates that these two cations displace the layer of waters on top of CO$_{ads}$. The waters identified by their characteristic O—D stretch frequency at $\approx$2,710 cm^{-1} are predisposed to hydrogen bond to the terminal oxygens of the CO dimer, a key intermediate in the formation of ethylene (48, 84–87, 122, 123). In line with recent theoretical predictions (87), our experimental results suggest that hydrogen bonding of water to the CO dimer is critical for its formation.

Materials and Methods

Materials. For Cu thin-film deposition on Si, NH$_4$F (40 wt% in H$_2$O) and HF (48 wt%) were purchased from Fisher Scientific. CuSO$_4$·5H$_2$O (99.999%; trace metal basis), EDTA-Na$_2$ (99.0–101.0%; ACS Reagent), 2,2-bipyridine ($\geq$99%; ReagentPlus), HCHO (35 wt%; 10% methanol as stabilizer), and NaOH (99.99%; trace metals basis) were acquired from Sigma Aldrich. Polycrystalline diamond pastes were procured from Ted Pella or Electron Microscopy Sciences.

For electrolyte preparation, tetramethylammonium chloride ($\geq$98%; Acros Organics), tetraethylammonium chloride (98%; Alfa Aesar), tetramethylammonium hydroxide pentahydrate (98%; Acros Organics), tetraethylammonium hydroxide (35 wt/wt% aqueous solution; Alfa Aesar), tetrapropylammonium hydroxide (25% in water; Acros Organics), tetrabutylammonium hydroxide (40 wt%; Acros Organics), boric acid (Puratronic 99.9995%; Alfa Aesar), and deuterium oxide (99.8 atom% D; Acros Organics) were purchased from Fisher Scientific. Tetrapropylammonium chloride (98%) and tetrabutylammonium chloride ($\geq$97%) were obtained from Sigma Aldrich. Deuterated tetramethylammonium chloride (D12, $\geq$98%) was obtained from Cambridge Isotope Laboratories.

Ar (ultrahigh purity), N$_2$ (ultrahigh purity), and CO (99.999%) were obtained from Air Gas.

DEMS System. The DEMS setup (*SI Appendix*, Fig. S1) was designed on the basis of prior reports (124–126). The reaction products that evolved from the electrode/electrolyte interface were collected by a sampling tip positioned $\approx$0.5 mm above the electrode surface. The sampling tip consisted of a polyether ether ketone (PEEK) tube plugged by a porous polytetrafluoroethylene (PTFE) cylinder with a pore size of $\approx$10 μm, a diameter of $\approx$3 mm, and a height of $\approx$2 mm (Genuine Porex). To provide a watertight seal, the cylinder was epoxied into the PEEK tube. A PTFE membrane of 20 nm pore size (PF-002HS; Cobetter Laboratory) was wrapped around the PEEK tube/PTFE cylinder assembly and was fixated with epoxy and shrink tubing.

The tip was connected through PEEK tubing to a detection chamber that contained a residual gas analyzer (Microvision 2; MKS Instruments). The chamber was pumped by a turbomolecular pump with a pumping speed of 67 L·s^{-1} (HiCube 80 Eco; Pfeiffer Vacuum). A needle valve formed an adjustable orifice that separated the tip assembly from the vacuum chamber. The pressure before the needle valve ($\approx$0.1 torr) was controlled by a dry scroll pump (Edwards nXDS 6i; Edwards Vacuum). During the measurement, the pressure inside the detection chamber was $\approx$10^{-5} torr.

Cu Foil Preparation. Before each DEMS measurement, the copper foil (Puratronic 99.999%, 1.0 mm; Alfa Aesar) was first polished with a 1,500-grit sandpaper to remove surface oxides. The surface was then hand polished with 1.0-μm and 0.3-μm alumina slurries. After each 10-min polishing step, the electrode was thoroughly rinsed with high-purity water. After 10 min of sonication in high-purity water, the copper foil was electropolished in an H$_3$PO$_4$, H$_2$O, and H$_2$SO$_4$ bath with volume ratio 10:5:2. The copper foil was subjected to a potential of 2.3 V vs. Cu for two sequential periods of 2 s, separated by an interval of 30 s at open circuit potential (127). Finally, the copper foil was rinsed thoroughly with high-purity water and blow-dried with N$_2$. Before each DEMS experiment, the copper foil was subjected to cleaning voltammetric cycles. A surface roughness factor of $\approx$3 compared with a smooth Cu surface (128) was determined on the basis of electrochemical capacitance measurements. The electrochemical protocols are detailed in our prior report (99).

Electrochemical Methods for DEMS. Aqueous electrolytes containing 0.1 M alkyl$_4$N$^+$ hydroxide and 20 μM EDTA-Na$_2$ were titrated with H$_3$BO$_3$ to pH 9.5. The pH after the experiments was 9.5 ± 0.1. Measurements were performed in a single-compartment electrochemical cell with an electrolyte volume of 3 mL (*SI Appendix*, Fig. S1). A VersaStat3 potentiostat (AMETEK) controlled the potential. A Pt foil (Premion 99.99%, 0.025 mm; Alfa Aesar) and a leak-free Ag/AgCl electrode (ET072, 3.4 M KCl; eDAQ) were used as the counter and reference electrodes, respectively. Before each experiment, the Pt foil was soaked in an aqueous acid solution (30 wt% H$_2$SO$_4$, 30 wt% HNO$_3$) for 1 h and was then rinsed with high-purity water. The Ag/AgCl reference electrode was regularly calibrated with respect to a saturated calomel electrode (CHI 150; CH Instruments, Inc.). The measured potential was converted to the SHE scale according to $V_{SHE} = V_{Ag/AgCl} + 0.209$ V. Seventy-six percent of the solution resistance was compensated in situ with the VersaStat3 potentiostat. The geometric surface area of the electrode was $\approx$1.9 cm^2.

The sequence of potential steps during DEMS measurements is described in the main text. Before the potential was applied, the electrolyte was purged with Ar at a rate of 5 sccm for 10 min. A voltammetric cycle from −0.39 V to −0.99 V with 10 mV·s^{-1} was carried out, and then the potential was held at −0.39 V for 20 min under CO purging at a rate of 5 sccm. Mass spectra were recorded with a time resolution of $\approx$3 s. For each partial pressure trace, the value that was recorded about 30 s before time 0 (the time of the first potential step, Fig. 1) was subtracted from the trace to zero out the baseline. Each trace in Fig. 1 was smoothed by a

binomial algorithm and is the average of two independent measurements. The background-subtracted, unsmoothed raw data are shown in *SI Appendix*, Figs. S17–S20.

Cu Thin-Film Preparation for SEIRAS. Thin polycrystalline Cu films were deposited on a reflecting facet of a 60° Si prism (Pike Technologies) by an electroless deposition procedure and characterized as described in our previous report (99). The film roughness factor was ≈13. The roughness of the films was maintained between ±20% of the original value after the spectroelectrochemical measurements. The typical surface morphology of the films was characterized by atomic force microscopy (*SI Appendix*, Fig. S9). Characterization by X-ray photoelectron spectroscopy was reported in our prior study (99).

Electrochemical Methods for SEIRAS. For the spectroelectrochemical measurements shown in the main text, the electrolyte was prepared with D_2O. The initial pH of the electrolyte was 9.7 ± 0.5. After the experiments, the pH typically decreased by ≈10%. Measurements were performed in a single-compartment electrochemical cell (*SI Appendix*, Fig. S7) with 4 mL electrolyte. The electrical connection from the film to the potentiostat was made by sandwiching a ring of Cu foil (Puratronic 99.999%, 0.025 mm; Alfa Aesar) between the circular edge of the film and a Viton O-ring from the PEEK electrochemical cell. A Au wire (99.999%, 0.5 mm; Alfa Aesar) and a Ag/AgCl electrode (RE-5B, 3 M NaCl; BASi Inc.) were used as the counter and

reference electrodes, respectively. The Cu ring and Au wire were polished with 0.3 μm alumina slurry for 5 min and were then rinsed with high-purity water. The Ag/AgCl reference electrode was calibrated as described above. The geometric surface area of the Cu thin film was ≈1.9 cm². The Cu thin film was first held at −0.39 V for 20 min for CO saturation, and the potential was then linearly swept to −1.49 V at a rate of 2 mV·s⁻¹. The cell resistance was not compensated.

SEIRAS Measurements. The Si crystal coated with the Cu thin film was assembled into a PEEK electrochemical cell, which was placed on an ATR accessory (VeeMax III; Pike Technologies). Spectra were recorded with a nitrogen-purged Bruker Vertex 70 FTIR spectrometer equipped with a liquid nitrogen-cooled photoconductive mercury cadmium telluride (MCT) detector (FTIR-16; Infrared Associates). Spectra were collected every 4.61 s with a spectral resolution of 4 cm⁻¹ and a scanner velocity of 40 kHz. The change in optical density was calculated according to $mOD = -10^3 \cdot \log(S/R)$, with S and R referring to the single-beam sample spectrum and the single-beam reference spectrum, respectively. The reference potential was −0.39 V. To determine accurately the peak frequency, a cubic spline was used to interpolate between recorded data points (*SI Appendix*, Fig. S21).

1. Chen P, Meyer TJ (1998) Medium effects on charge transfer in metal complexes. *Chem Rev* 98:1439–1478.
2. Velsko SP, Waldeck DH, Fleming GR (1983) Breakdown of Kramers theory description of photochemical isomerization and the possible involvement of frequency dependent friction. *J Chem Phys* 78:249–258.
3. Mukherjee S, Waegele MM, Chowdhury P, Guo L, Gai F (2009) Effect of macromolecular crowding on protein folding dynamics at the secondary structure level. *J Mol Biol* 393:227–236.
4. Jorgensen WL, Blake JF, Lim D, Severance DL (1994) Investigation of solvent effects on pericyclic reactions by computer simulations. *J Chem Soc Faraday Trans* 90: 1727–1732.
5. Suydam IT, Snow CD, Pande VS, Boxer SG (2006) Electric fields at the active site of an enzyme: Direct comparison of experiment with theory. *Science* 313:200–204.
6. Breslow R, Maitra U (1984) On the origin of product selectivity in aqueous Diels-Alder reactions. *Tetrahedron Lett* 25:1239–1240.
7. Rybtchinski B, Milstein D (1999) Solvent-controlled selectivity toward exclusive C-C or C-H bond activation by a cationic metal center. *J Am Chem Soc* 121:4528–4529.
8. Grote RF, Van der Zwan G, Hynes JT (1984) Frequency-dependent friction and solution reaction rates. *J Phys Chem* 88:4676–4684.
9. Weaver MJ (1992) Dynamical solvent effects on activated electron-transfer reactions: Principles, pitfalls, and progress. *Chem Rev* 92:463–480.
10. Hori Y, Murata A, Takahashi R (1989) Formation of hydrocarbons in the electrochemical reduction of carbon dioxide at a copper electrode in aqueous solution. *J Chem Soc Faraday Trans* 1:2309–2326.
11. Gattrell M, Gupta N, Co A (2006) A review of the aqueous electrochemical reduction of CO_2 to hydrocarbons at copper. *J Electroanal Chem* 594:1–19.
12. Hori Y (2008) *Electrochemical CO_2 Reduction on Metal Electrodes* (Springer, New York), pp 89–189.
13. Kuhl KP, Cave ER, Abram DN, Jaramillo TF (2012) New insights into the electrochemical reduction of carbon dioxide on metallic copper surfaces. *Energy Environ Sci* 5:7050–7059.
14. Kuhl KP, et al. (2014) Electrocatalytic conversion of carbon dioxide to methane and methanol on transition metal surfaces. *J Am Chem Soc* 136:14107–14113.
15. Hoang TTH, Ma S, Gold JI, Kenis PJA, Gewirth AA (2017) Nanoporous copper films by additive-controlled electrodeposition: CO_2 reduction catalysis. *ACS Catal* 7:3313–3321.
16. Weng Z, et al. (2017) Self-cleaning catalyst electrodes for stabilized CO_2 reduction to hydrocarbons. *Angew Chem Inter Ed* 56:13135–13139.
17. Dunwell M, Yan Y, Xu B (2018) Understanding the influence of the electrochemical double-layer on heterogeneous electrochemical reactions. *Curr Opin Chem Eng* 20:151–158.
18. Arán-Ais RM, Gao D, Roldan Cuenya B (2018) Structure- and electrolyte-sensitivity in CO_2 electroreduction. *Acc Chem Res* 51:2906–2917.
19. Li CW, Ciston J, Kanan MW (2014) Electroreduction of carbon monoxide to liquid fuel on oxide-derived nanocrystalline copper. *Nature* 508:504–507.
20. Mariano RG, McKelvey K, White HS, Kanan MW (2017) Selective increase in CO_2 electroreduction activity at grain-boundary surface terminations. *Science* 358:1187–1192.
21. Cao L, et al. (2017) Mechanistic insights for low-overpotential electroreduction of CO_2 to CO on copper nanowires. *ACS Catal* 7:8578–8587.
22. Raciti D, et al. (2017) Low-overpotential electroreduction of carbon monoxide using copper nanowires. *ACS Catal* 7:4467–4472.
23. Clark EL, Hahn C, Jaramillo TF, Bell AT (2017) Electrochemical CO_2 reduction over compressively strained CuAg surface alloys with enhanced multi-carbon oxygenate selectivity. *J Am Chem Soc* 139:15848–15857.
24. Choi C, et al. (2018) A highly active star decahedron Cu nanocatalyst for hydrocarbon production at low overpotentials. *Adv Mater* 31:1805405.
25. Mistry H, et al. (2014) Exceptional size-dependent activity enhancement in the electroreduction of CO_2 over Au nanoparticles. *J Am Chem Soc* 136:16473–16476.
26. Manthiram K, Beberwyck BJ, Alivisatos AP (2014) Enhanced electrochemical methanation of carbon dioxide with a dispersible nanoscale copper catalyst. *J Am Chem Soc* 136:13319–13325.
27. Reske R, Mistry H, Behafarid F, Cuenya BR, Strasser P (2014) Particle size effects in the catalytic electroreduction of CO_2 on Cu nanoparticles. *J Am Chem Soc* 136: 6978–6986.
28. Hori Y, Takahashi I, Koga O, Hoshi N (2003) Electrochemical reduction of carbon dioxide at various series of copper single crystal electrodes. *J Mol Catal A Chem* 199:39–47.
29. Loiudice A, et al. (2016) Tailoring copper nanocrystals towards C_2 products in electrochemical CO_2 reduction. *Angew Chem Int Ed* 55:5789–5792.
30. Hahn C, et al. (2017) Engineering Cu surfaces for the electrocatalytic conversion of CO_2: Controlling selectivity toward oxygenates and hydrocarbons. *Proc Natl Acad Sci USA* 114:5918–5923.
31. Schouten KJP, Qin Z, Pérez Gallent E, Koper MTM (2012) Two pathways for the formation of ethylene in CO reduction on single-crystal copper electrodes. *J Am Chem Soc* 134:9864–9867.
32. Huang Y, Handoko AD, Hirunsit P, Yeo BS (2017) Electrochemical reduction of CO_2 using copper single-crystal surfaces: Effects of CO^* coverage on the selective formation of ethylene. *ACS Catal* 7:1749–1756.
33. Rosen BA, et al. (2011) Ionic liquid–mediated selective conversion of CO_2 to CO at low overpotentials. *Science* 334:643–644.
34. Figueiredo MC, Ledezma-Yanez I, Koper MTM (2016) In situ spectroscopic study of CO_2 electroreduction at copper electrodes in acetonitrile. *ACS Catal* 6:2382–2392.
35. García Rey N, Dlott DD (2017) Effects of water on low-overpotential CO_2 reduction in ionic liquid studied by sum-frequency generation spectroscopy. *Phys Chem Chem Phys* 19:10491–10501.
36. Schreier M, Yoon Y, Jackson MN, Surendranath Y (2018) Competition between H and CO for active sites governs copper-mediated electrosynthesis of hydrocarbon fuels. *Angew Chem Int Ed* 57:10221–10225.
37. McCrum IT, Hickner MA, Janik MJ (2018) Quaternary ammonium cation specific adsorption on platinum electrodes: A combined experimental and density functional theory study. *J Electrochem Soc* 165:F114–F121.
38. Varela AS, Ju W, Reier T, Strasser P (2016) Tuning the catalytic activity and selectivity of Cu for CO_2 electroreduction in the presence of halides. *ACS Catal* 6:2136–2144.
39. Akhade SA, McCrum IT, Janik MJ (2016) The impact of specifically adsorbed ions on the copper-catalyzed electroreduction of CO_2. *J Electrochem Soc* 163:F477–F484.
40. Paik W., Andersen TN, Eyring H (1969) Kinetic studies of the electrolytic reduction of carbon dioxide on the mercury electrode. *Electrochim Acta* 14:1217–1232.
41. Hori Y, Suzuki S (1982) Electrolytic reduction of carbon dioxide at mercury electrode in aqueous solution. *Bull Chem Soc Jpn* 55:660–665.
42. Murata A, Hori Y (1991) Product selectivity affected by cationic species in electrochemical reduction of CO_2 and CO at a Cu electrode. *Bull Chem Soc Jpn* 64:123–127.
43. Thorson MR, Siil KI, Kenis PJA (2013) Effect of cations on the electrochemical conversion of CO_2 to CO. *J Electrochem Soc* 160:F69–F74.
44. Sun L, Ramesha GK, Kamat PV, Brennecke JF (2014) Switching the reaction course of electrochemical CO_2 reduction with ionic liquids. *Langmuir* 30:6302–6308.
45. Singh MR, Kwon Y, Lum Y, Ager JW, Bell AT (2016) Hydrolysis of electrolyte cations enhances the electrochemical reduction of CO_2 over Ag and Cu. *J Am Chem Soc* 138:13006–13012.

CHEMISTRY

46. Chen LD, Urushihara M, Chan K, Nørskov JK (2016) Electric field effects in electrochemical CO$_2$ reduction. *ACS Catal* 6:7133–7139.

47. Resasco J, et al. (2017) Promoter effects of alkali metal cations on the electrochemical reduction of carbon dioxide. *J Am Chem Soc* 139:11277–11287.

48. Pérez-Gallent E, Marcandalli G, Figueiredo MC, Calle-Vallejo F, Koper MTM (2017) Structure- and potential-dependent cation effects on CO reduction at copper single-crystal electrodes. *J Am Chem Soc* 139:16412–16419.

49. Feaster JT, et al. (2017) Understanding the influence of [EMIM]Cl on the suppression of the hydrogen evolution reaction on transition metal electrodes. *Langmuir* 33:9464–9471.

50. Ayemoba O, Cuesta A (2017) Spectroscopic evidence of size-dependent buffering of interfacial pH by cation hydrolysis during CO$_2$ electroreduction. *ACS Appl Mater Interf* 9:27377–27382.

51. Sartin MM, et al. (2018) Effect of particle shape and electrolyte cation on CO adsorption to copper oxide nanoparticle electrocatalysts. *J Phys Chem C* 122:26489–26498.

52. Hori Y, Takahashi R, Yoshinami Y, Murata A (1997) Electrochemical reduction of CO at a copper electrode. *J Phys Chem B* 101:7075–7081.

53. Singh MR, Clark EL, Bell AT (2015) Effects of electrolyte, catalyst, and membrane composition and operating conditions on the performance of solar-driven electrochemical reduction of carbon dioxide. *Phys Chem Chem Phys* 17:18924–18936.

54. Varela AS, Kroschel M, Reier T, Strasser P (2016) Controlling the selectivity of CO$_2$ electroreduction on copper: The effect of the electrolyte concentration and the importance of the local pH. *Catal Today* 260:8–13.

55. Wuttig A, et al. (2016) Tracking a common surface-bound intermediate during CO$_2$-to-fuels catalysis. *ACS Cent Sci* 2:522–528.

56. Seifitokaldani A, et al. (2018) Hydronium-induced switching between CO$_2$ electroreduction pathways. *J Am Chem Soc* 140:3833–3837.

57. Wang L, et al. (2018) Electrochemical carbon monoxide reduction on polycrystalline copper: Effects of potential, pressure, and pH on selectivity toward multicarbon and oxygenated products. *ACS Catal* 8:7445–7454.

58. Dunwell M, et al. (2018) Examination of near-electrode concentration gradients and kinetic impacts on the electrochemical reduction of CO$_2$ using surface-enhanced infrared spectroscopy. *ACS Catal* 8:3999–4008.

59. Barton Cole E, et al. (2010) Using a one-electron shuttle for the multielectron reduction of CO$_2$ to methanol: Kinetic, mechanistic, and structural insights. *J Am Chem Soc* 132:11539–11551.

60. Oberst JL, Jhong H-R, Kenis PJA, Gewirth AA (2016) Insight into the electrochemical reduction of CO$_2$ on gold via surface-enhanced Raman spectroscopy and N-containing additives. *J Solid State Electrochem* 20:1149–1154.

61. Fang Y, Flake JC (2017) Electrochemical reduction of CO$_2$ at functionalized Au electrodes. *J Am Chem Soc* 139:3399–3405.

62. Ahn S, et al. (2018) Poly-amide modified copper foam electrodes for enhanced electrochemical reduction of carbon dioxide. *ACS Catal* 8:4132–4142.

63. Atifi A, Boyce DW, DiMeglio JL, Rosenthal J (2018) Directing the outcome of CO$_2$ reduction at bismuth cathodes using varied ionic liquid promoters. *ACS Catal* 8:2857–2863.

64. Frumkin AN (1959) Influence of cation adsorption on the kinetics of electrode processes. *Trans Faraday Soc* 55:156–167.

65. Mills JN, McCrum IT, Janik MJ (2014) Alkali cation specific adsorption onto fcc(111) transition metal electrodes. *Phys Chem Chem Phys* 16:13699–13707.

66. Liu M, et al. (2016) Enhanced electrocatalytic CO$_2$ reduction via field-induced reagent concentration. *Nature* 537:382–386.

67. Herasymenko P, Šlendyk I (1930) Wasserstoffüberspannung und adsorption der ionen [Hydrogen evolution overpotential and adsorption of ions]. *Z Phys Chem A* 149:123–139. German.

68. Ikeda O, Tamura H, Matsuda Y (1980) Specific adsorption effects of organic cation on the electroreduction of dimethylfumarate. *J Electroanal Chem* 111:345–358.

69. Fawcett WR, Fedurco M, Opallo M (1992) The inhibiting effects of tetraalkylammonium cations on simple heterogeneous electron transfer reactions in polar aprotic solvents. *J Phys Chem* 96:9959–9964.

70. Strmcnik D, et al. (2009) The role of non-covalent interactions in electrocatalytic fuel-cell reactions on platinum. *Nat Chem* 1:466–472.

71. Strmcnik D, et al. (2011) Effects of Li$^+$, K$^+$, and Ba^{2+} cations on the ORR at model and high surface area Pt and Au surfaces in alkaline solutions. *J Phys Chem Lett* 2:2733–2736.

72. Fedurco M., Kedzierzawski P., Augustynski J. (1999) Effect of multivalent cations upon reduction of nitrate ions at the Ag electrode. *J Electrochem Soc* 146:2569–2572.

73. Stoffelsma C, et al. (2010) Promotion of the oxidation of carbon monoxide at stepped platinum single-crystal electrodes in alkaline media by lithium and beryllium cations. *J Am Chem Soc* 132:16127–16133.

74. Subbaraman R, et al. (2011) Enhancing hydrogen evolution activity in water splitting by tailoring Li$^+$-Ni(OH)$_2$-Pt interfaces. *Science* 334:1256–1260.

75. Suntivich J, Perry EE, Gasteiger HA, Shao-Horn Y (2013) The influence of the cation on the oxygen reduction and evolution activities of oxide surfaces in alkaline electrolyte. *Electrocatal* 4:49–55.

76. van der Vliet DF, Koper MTM (2010) Electrochemistry of Pt (100) in alkaline media: A voltammetric study. *Surf Sci* 604:1912–1918.

77. Yamakata A, Soeta E, Ishiyama T, Osawa M, Morita A (2013) Real-time observation of the destruction of hydration shells under electrochemical force. *J Am Chem Soc* 135:15033–15039.

78. Yamakata A, Osawa M (2017) Cation-dependent restructure of the electric double layer on CO-covered Pt electrodes: Difference between hydrophilic and hydrophobic cations. *J Electroanal Chem* 800:19–24.

79. Marcus Y (2008) Tetraalkylammonium ions in aqueous and non-aqueous solutions. *J Solution Chem* 37:1071–1098.

80. Pearson RG (1988) Absolute electronegativity and hardness: Application to inorganic chemistry. *Inorg Chem* 27:734–740.

81. Roth JD, Weaver MJ (1992) Role of the double-layer cation on the potential-dependent stretching frequencies and binding geometries of carbon monoxide at platinum-nonaqueous interfaces. *Langmuir* 8:1451–1458.

82. Durand WJ, Peterson AA, Studt F, Abild-Pedersen F, Nørskov JK (2011) Structure effects on the energetics of the electrochemical reduction of CO$_2$ by copper surfaces. *Surf Sci* 605:1354–1359.

83. Nie X, Esopi MR, Janik MJ, Asthagiri A (2013) Selectivity of CO$_2$ reduction on copper electrodes: The role of the kinetics of elementary steps. *Angew Chem Int Ed* 52:2459–2462.

84. Calle-Vallejo F, Koper MTM (2013) Theoretical considerations on the electroreduction of CO to C$_2$ species on Cu(100) electrodes. *Angew Chem Int Ed* 52:7282–7285.

85. Goodpaster JD, Bell AT, Head-Gordon M (2016) Identification of possible pathways for C-C bond formation during electrochemical reduction of CO$_2$: New theoretical insights from an improved electrochemical model. *J Phys Chem Lett* 7:1471–1477.

86. Xiao H, Cheng T, Goddard WA (2017) Atomistic mechanisms underlying selectivities in C$_1$ and C$_2$ products from electrochemical reduction of CO on Cu(111). *J Am Chem Soc* 139:130–136.

87. Bagger A, Arnarson L, Hansen MH, Spohr E, Rossmeisl J (2019) Electrochemical CO reduction: A property of the electrochemical interface. *J Am Chem Soc* 141:1506–1514.

88. Wuttig A, Surendranath Y (2015) Impurity ion complexation enhances carbon dioxide reduction catalysis. *ACS Catal* 5:4479–4484.

89. Roberts FS, Kuhl KP, Nilsson A (2015) High selectivity for ethylene from carbon dioxide reduction over copper nanocube electrocatalysts. *Angew Chem Int Ed* 54:5179–5182.

90. Hori Y, Murata A, Takahashi R, Suzuki S (1987) Electrochemical reduction of carbon monoxide to hydrocarbons at various metal electrodes in aqueous solution. *Chem Lett* 16:1665–1668.

91. White JL, et al. (2015) Light-driven heterogeneous reduction of carbon dioxide: Photocatalysts and photoelectrodes. *Chem Rev* 115:12888–12935.

92. Wang F, et al. (2007) Seeded growth fabrication of Cu-on-Si electrodes for in situ ATR-SEIRAS applications. *Electrochim Acta* 52:5950–5957.

93. Gunathunge CM, et al. (2017) Spectroscopic observation of reversible surface reconstruction of copper electrodes under CO$_2$ reduction. *J Phys Chem C* 121:12337–12344.

94. Conway BE (1960) Kinetics of electrolytic hydrogen and deuterium evolution. *Proc R Soc Lond Ser A* 256:128–144.

95. Gunathunge CM, Ovalle VJ, Waegele MM (2017) Probing promoting effects of alkali cations on the reduction of CO at the aqueous electrolyte/copper interface. *Phys Chem Chem Phys* 19:30166–30172.

96. Hori Y, Koga O, Yamazaki H, Matsuo T (1995) Infrared spectroscopy of adsorbed CO and intermediate species in electrochemical reduction of CO$_2$ to hydrocarbons on a Cu electrode. *Electrochim Acta* 40:2617–2622.

97. Koga O, et al. (2005) Infrared spectroscopic and voltammetric study of adsorbed CO on stepped surfaces of copper monocrystalline electrodes. *Electrochim Acta* 50:2475–2485.

98. Dunwell M., Wang J, Yan Y, Xu B (2017) Surface enhanced spectroscopic investigations of adsorption of cations on electrochemical interfaces. *Phys Chem Chem Phys* 19:971–975.

99. Gunathunge CM, Ovalle VJ, Li Y, Janik MJ, Waegele MM (2018) Existence of an electrochemically inert CO population on Cu electrodes in alkaline pH. *ACS Catal* 8:7507–7516.

100. Ueba H (1987) Chemical effects on vibrational properties of adsorbed molecules on metal surfaces: Coverage dependence. *Surf Sci* 188:421–455.

101. Bublitz GU, Boxer SG (1997) Stark spectroscopy: Applications in chemistry, biology, and materials science. *Annu Rev Phys Chem* 48:213–242.

102. Sorenson SA, Patrow JG, Dawlaty JM (2017) Solvation reaction field at the interface measured by vibrational sum frequency generation spectroscopy. *J Am Chem Soc* 139:2369–2378.

103. Ge A, et al. (2017) Interfacial structure and electric field probed by in situ electrochemical vibrational Stark effect spectroscopy and computational modeling. *J Phys Chem C* 121:18674–18682.

104. Clark ML, et al. (2018) CO$_2$ reduction catalysts on gold electrode surfaces influenced by large electric fields. *J Am Chem Soc* 140:17643–17655.

105. Lambert DK (1988) Vibrational Stark effect of CO on Ni(100), and CO in the aqueous double layer: Experiment, theory, and models. *J Chem Phys* 89:3847–3860.

106. Bagus PS, Nelin CJ, Müller W, Philpott MR, Seki H (1987) Field-induced vibrational frequency shifts of CO and CN chemisorbed on Cu(100). *Phys Rev Lett* 58:559–562.

107. Vetter KJ (1967) *Electrochemical Kinetics, Theoretical Aspects* (Academic, New York).

108. Anderson MR, Huang J (1991) The influence of cation size upon the infrared spectrum of carbon monoxide adsorbed on platinum electrodes. *J Electroanal Chem* 318:335–347.

109. Jiang X, Weaver MJ (1992) The role of interfacial potential in adsorbate bonding: Electrode potential-dependent infrared spectra for saturated CO adlayers on Pt(110) and related electrochemical surfaces in varying solvent environments. *Surf Sci* 275:237–252.

110. Andersson S, Pendry JB (1979) Structure of CO adsorbed on Cu(100) and Ni(100). *Phys Rev Lett* 43:363–366.

111. Łukomska A, Sobkowski J (2004) Potential of zero charge of monocrystalline copper electrodes in perchlorate solutions. *J Electroanal Chem* 567:95–102.
112. Gileadi E, Argade SD, Bockris JO'M (1966) The potential of zero charge of platinum and its pH dependence. *J Phys Chem* 70:2044–2046.
113. Che F, et al. (2018) Elucidating the roles of electric fields in catalysis: A perspective. *ACS Catal* 8:5153–5174.
114. Atkins P, de Paula J (2002) *Atkins' Physical Chemistry* (Oxford Univ Press, Oxford).
115. Vollmer S, Witte G, Wöll C (2001) Determination of site specific adsorption energies of CO on copper. *Catal Lett* 77:97–101.
116. Verdaguer-Casadevall A, et al. (2015) Probing the active surface sites for CO reduction on oxide-derived copper electrocatalysts. *J Am Chem Soc* 137:9808–9811.
117. Kizhakevariam N, Jiang X, Weaver MJ (1994) Infrared spectroscopy of model electrochemical interfaces in ultrahigh vacuum: The archetypical case of carbon monoxide/water coadsorption on Pt(111). *J Chem Phys* 100:6750–6764.
118. Ogasawara H, Yoshinobu J, Kawai M (1997) Direct observation of the molecular interaction between chemisorbed CO and water overlayer on Pt(111). *Surf Sci* 386:73–77.
119. Yan Y-G, et al. (2005) Ubiquitous strategy for probing ATR surface-enhanced infrared absorption at platinum group metal-electrolyte interfaces. *J Phys Chem B* 109:7900–7906.
120. Nagao M, Watanabe K, Matsumoto Y (2009) Ultrafast vibrational energy transfer in the layers of D_2O and CO on Pt(111) studied with time-resolved sum-frequency-generation spectroscopy. *J Phys Chem C* 113:11712–11719.
121. Yan Y-G, et al. (2011) Interfacial water at a CO-predosed platinum electrode: A surface enhanced infrared study with strong hydrogen evolution reaction control. *J Phys Chem C* 115:5584–5592.
122. Cheng T, Xiao H, Goddard WA (2017) Full atomistic reaction mechanism with kinetics for CO reduction on Cu(100) from ab initio molecular dynamics free-energy calculations at 298 K. *Proc Natl Acad Sci USA* 114:1795–1800.
123. Pérez-Gallent E, Figueiredo MC, Calle-Vallejo F, Koper MTM (2017) Spectroscopic observation of a hydrogenated CO dimer intermediate during CO reduction on Cu(100) electrodes. *Angew Chem Int Ed* 56:3621–3624.
124. Wonders AH, Housmans THM, Rosca V, Koper MTM (2006) On-line mass spectrometry system for measurements at single-crystal electrodes in hanging meniscus configuration. *J Appl Electrochem* 36:1215–1221.
125. Jambunathan K, Hillier AC (2003) Measuring electrocatalytic activity on a local scale with scanning differential electrochemical mass spectrometry. *J Electrochem Soc* 150:E312–E320.
126. Grote J-P, Zeradjanin AR, Cherevko S, Mayrhofer KJJ (2014) Coupling of a scanning flow cell with online electrochemical mass spectrometry for screening of reaction selectivity. *Rev Sci Instrum* 85:104101.
127. Schouten KJP, Kwon Y, van der Ham CJM, Qin Z, Koper MTM (2011) A new mechanism for the selectivity to C_1 and C_2 species in the electrochemical reduction of carbon dioxide on copper electrodes. *Chem Sci* 2:1902–1909.
128. Waszczuk P, Zelenay P, Sobkowski J (1995) Surface interaction of benzoic acid with a copper electrode. *Electrochim Acta* 40:1717–1721.

CHEMISTRY